Lithium Isotope History of Cenozoic Seawater: Changes in Silicate Weathering and Reverse Weathering

Sambuddha Misra[1]*† and Philip N. Froelich[2]

Weathering of uplifted continental rocks consumes carbon dioxide and transports cations to the oceans, thereby playing a critical role in controlling both seawater chemistry and climate. However, there are few archives of seawater chemical change that reveal shifts in global tectonic forces connecting Earth ocean-climate processes. We present a 68-million-year record of lithium isotopes in seawater (δ^7Li_{SW}) reconstructed from planktonic foraminifera. From the Paleocene (60 million years ago) to the present, δ^7Li_{SW} rose by 9 per mil (‰), requiring large changes in continental weathering and seafloor reverse weathering that are consistent with increased tectonic uplift, more rapid continental denudation, increasingly incongruent continental weathering (lower chemical weathering intensity), and more rapid CO_2 drawdown. A 5‰ drop in δ^7Li_{SW} across the Cretaceous-Paleogene boundary cannot be produced by an impactor or by Deccan trap volcanism, suggesting large-scale continental denudation.

Lithium, the lightest of the alkali elements, is a conservative cation in seawater. The residence time of Li in seawater (~1.2 million years) is much shorter than for the other major alkalis (Na^+ and K^+) but is much longer than the oceanic mixing time (~1000 years), so that Li in seawater is well mixed and homogeneous vertically and laterally in both concentration (ratio to salt) and in isotopic composition ($[Li]_{SW} \approx 26$ μM; $\delta^7Li_{SW} = 31$‰) (*1*) (fig. S1). Lithium is a trace component in continental and seafloor rocks, and unlike other recorders of oceanic chemistry changes (namely Sr and Os), it is hosted almost exclusively in silicate minerals. Because of the large relative mass difference between its two stable isotopes (^6Li and ^7Li), low-temperature Li isotope fractionation exhibits a very large range, making Li a powerful tracer of low-temperature geochemical processes. Among continental granites, mid-ocean ridge basalt (MORB), marine authigenic aluminosilicate clays (MAACs), dissolved Li sources and sinks to and from the sea, and seawater itself, the spread in δ^7Li values is more than 31‰—an enormous isotopic range.

The Li isotopic composition of seawater reflects a balance between input and removal fluxes and their isotopic compositions. The two dominant sources of dissolved Li to seawater are rivers (low-temperature chemical weathering of continental silicate rocks) and hydrothermal (HT) fluxes from mid-ocean ridge spreading centers (high-temperature weathering of oceanic silicate rocks) (*2*–*6*). The removal of Li from seawater is entirely by incorporation into marine sediments and low-temperature altered oceanic crust (AOC) via formation of Li-, Mg-, and Fe-bearing MAACs ("reverse weathering") (*7*–*13*) (Fig. 1 and Table 1). The ^7Li enrichment of seawater (much heavier than all sources) requires the existence of marine reverse weathering that produces secondary clays bearing Li that is isotopically much lighter than

[1]Geochemistry Group, National High Magnetic Field Laboratory, and Department of Earth, Ocean and Atmospheric Sciences, Florida State University, Tallahassee, FL 32310, USA. [2]Froelich Education Services, 3402 Cameron Chase Drive, Tallahassee, FL 32309, USA.

*Present address: Department of Earth Sciences, University of Cambridge, Cambridge CB2 3EQ, UK.
†To whom correspondence should be addressed. E-mail: sm929@cam.ac.uk

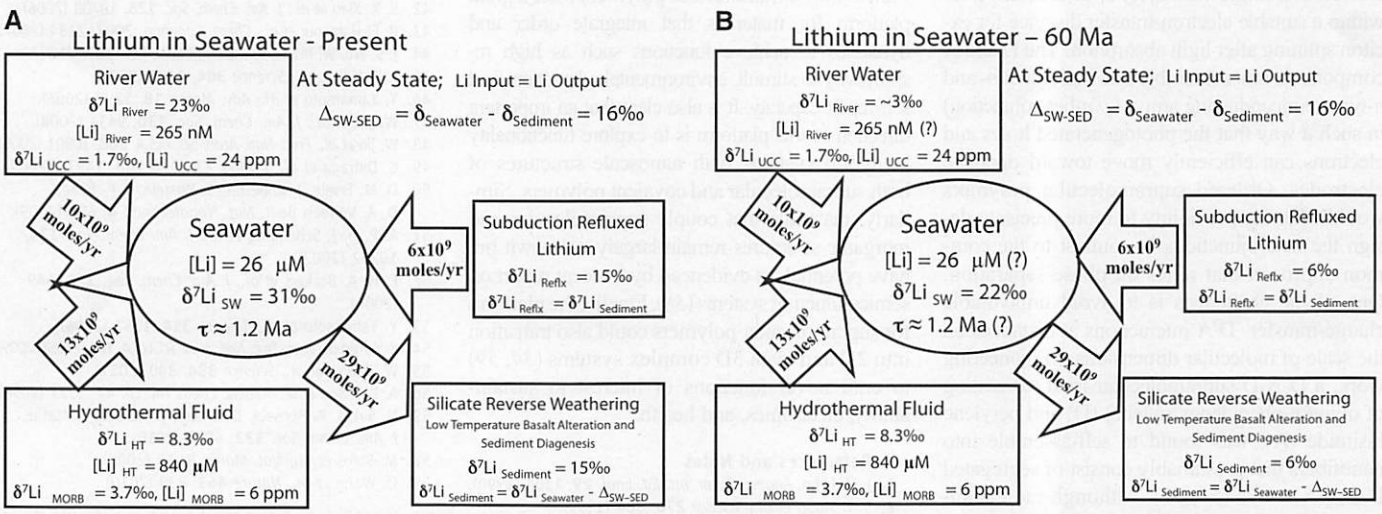

Fig. 1. (**A**) Box model of Li cycle in modern ocean (Table 1). At steady state, the input and output fluxes and isotopic compositions balance each other. The total input flux of Li to the ocean (F_{Input}) is the sum of riverine (F_{Riv}), hydrothermal (F_{HT}), and subduction reflux (F_{Reflx}). The outgoing flux (F_{Sink}) is the sum of Li removal via MAAC and AOC formation during reverse weathering. The mass balance is numerically expressed as $F_{Input} = F_{Riv} + F_{HT} + F_{Reflx} = F_{Sink}$. The isotopic composition of the input flux (δ^7Li_{Input}) is a flux-weighted average of the compositions of rivers (δ^7Li_{Riv}), hydrothermal fluids (δ^7Li_{HT}), and refluxed Li (δ^7Li_{Reflx}). The composition of the output flux (δ^7Li_{Sink}) is dependent on the seawater δ^7Li_{SW} value and has a constant offset from seawater ($\Delta_{Seawater-Sink} = \delta^7Li_{SW} - \delta^7Li_{Sink} = 16$‰). Steady-state isotope balance is expressed as $F_{Input} \times \delta^7Li_{Input} = F_{Sink} \times (\delta^7Li_{SW} - \Delta_{SW-Sink})$. (**B**) One possible steady-state isotope mass balance for the Paleocene-Eocene (P-E) Ocean (60 Ma) when δ^7Li_{SW} was 22‰, 9‰ lighter than today. F_{Riv} is set at modern values and δ^7Li_{Riv} is then constrained to lie near δ^7Li_{UCC}, reflecting congruent weathering of the peneplained transport-limited continents (*29*, *30*) plus perhaps dissolution of the basaltic Deccan Traps and North Atlantic Igneous Provinces. This P-E scenario is an end-member paradigm. Variants of this scenario in which river and hydrothermal fluxes are allowed to vary are explored in text S4 and fig. S10. These alternative scenarios demonstrate that the river condition is constrained to remain between 2‰ and 6‰ regardless of changes in river Li fluxes, hydrothermal fluxes, or seawater Li concentrations.

very large aspect ratio and have a uniform, open-ended hollow space that is 14 nm wide. The oxidized nanotube across a 180-nm–gap electrode displays an electrical conductivity of 2.5 megohms at 285 K (*45*). From a suspension of long nanotubes, it is possible to obtain a macroscopic fiber a few centimeters in length consisting of unidirectionally oriented nanotubes. Because of this alignment, the doped macroscopic fiber displays a clear anisotropy in electrical conductivity (*46*). Graphite-like supramolecular nanotubes with a variety of surface functional groups in their TEG termini can be fabricated through this strategy (for example, chemically reactive groups, metal-binding functions, and chromophores) (*47*). When an asymmetric center is incorporated into the ether side chains, nanotubes (*48*) and even nanocoils with one-handed helical chirality are formed. Didraga *et al.* reported the formation of a supramolecular nanotube with a bilayer wall based on a *J*-aggregated amphiphilic cyanine dye (*49*). By means of polarization-resolved near-field scanning optical microscopy, such a red-shifted exciton emission can be detected directly from a single piece of the supramolecular nanotube (*50*).

Photoconductive nanowires and device applications. One of the interesting functions for ordered electronically active supramolecular polymers would be photovoltaic activity. Although examples of such functional systems are still limited, work reported so far is creating a foundation and vision for this field (Fig. 4A). The nanowire polymers required must contain electron-donating (D) and accepting (A) components, either properly located in a single 1D object or in different ones within a suitable electron-transfer distance for exciton splitting after light absorption. The D and A components must assemble into individual *p*- and *n*-type semiconducting arrays (*p*/*n*-heterojunction) in such a way that the photogenerated holes and electrons can efficiently move toward opposite electrodes. Ordered supramolecular polymers would offer the possibility to more precisely design the heterojunctions in contrast to the common approach that relies on phase separation. One of the challenges is to avoid unfavorable charge-transfer D/A interactions at distances on the scale of molecular dimensions. In pioneering work, a D-A-D supramolecular triad, consisting of oligo(*p*-phenylenevinylene) (D) and perylene bisimide (A), was found to self-assemble into nanofibers that presumably consist of segregated D and A arrays (*51*, *52*). Although radical anions and cations could be generated photochemically in the nanofiber, they recombined within 60 ps (*51*).

Recently, a design strategy for photoconductive nanotubes with a coaxial *p*/*n*-heterojunction based on HBC units was successfully elaborated (*53*). In this supramolecular structure, a molecular layer of the electron acceptor trinitrofluorenone laminates a graphite-like tubular wall of HBC units that are electron donors (Fig. 4B). This coaxial *p*/*n*-heterojunction structure enables photocurrent generation with a large on/off ratio greater than 10^4 (Fig. 4C). It is interesting to note that at high concentrations of the building blocks, the anticipated charge-transfer interactions prevail, and only ill-defined microfibers form that hardly display a photocurrent (*53*). When a fullerene is used in these structures as the acceptor, the resultant carbon-rich coaxial nanotube shows, upon light illumination, an ambipolar charge-carrier transport profile, where the intratubular mobility is as large as the intersheet mobility in graphite. Furthermore, the nanotube shows a photovoltaic response (*54*), although the overall device performance is not satisfactory for practical use. More recently, this assembling strategy was extended to the formation of a graphite-like nanotube with a linear D/A heterojunction using a surface–cross-linked HBC nanotube as the seed and a fluorinated HBC as the monomer (*55*). Matile and co-workers proposed a zipper-type supramolecular copolymerization of positively and negatively charged D-A dyads from initiating groups immobilized on a gold substrate (*56*, *57*). This approach has the potential to yield aligned systems on electrode surfaces with many tunable properties. Generally speaking, a key issue to consider is the essential difficulty in aligning ordered supramolecular polymers unidirectionally over macroscopic length scales to create devices, and here is where approaches to hierarchical supramolecular structures described in the previous section could become useful.

Future Outlook

Functional supramolecular polymers offer a great platform for materials that integrate order and dynamics to achieve functions such as high responsivity to stimuli, environmental adaptation, and self-repair capacity. It is also clear that an important direction in this platform is to explore functionality in hybrid systems with nanoscale structures of both supramolecular and covalent polymers. Similarly, materials that couple supramolecular and inorganic structures remain largely unknown but have potential, as evidenced by a recent report on semiconducting systems (*58*). Finally, the platform for supramolecular polymers could also transition into 2D and even 3D complex systems (*34*, *59*) to craft novel functions of interest in sustainability, electronics, and health.

References and Notes

1. J. M. Lehn, *Angew. Chem. Int. Ed. Engl.* **29**, 1304 (1990).
2. S. I. Stupp *et al.*, *Science* **276**, 384 (1997).
3. G. B. Gardner, D. Venkataraman, J. S. Moore, S. Lee, *Nature* **374**, 792 (1995).
4. A. Ulman, *Chem. Rev.* **96**, 1533 (1996).
5. T. Kato, J. M. J. Frechet, *J. Am. Chem. Soc.* **111**, 8533 (1989).
6. B. G. G. Lohmeijer, U. S. Schubert, *Angew. Chem. Int. Ed.* **41**, 3825 (2002).
7. L. Henry, *Ann. Soc. Sci. Brux.* **3**, 267 (1878).
8. C. Fouquey, J.-M. Lehn, A.-M. Levelut, *Adv. Mater.* **2**, 254 (1990).
9. S. I. Stupp, S. Son, H. C. Lin, L. S. Li, *Science* **259**, 59 (1993).
10. T. F. A. De Greef *et al.*, *Chem. Rev.* **109**, 5687 (2009).
11. J. D. Hartgerink, J. R. Granja, R. A. Milligan, M. R. Ghadiri, *J. Am. Chem. Soc.* **118**, 43 (1996).
12. S. G. Zhang, *Nat. Biotechnol.* **21**, 1171 (2003).
13. R. P. Sijbesma *et al.*, *Science* **278**, 1601 (1997).
14. P. G. de Gennes, *J. Chem. Phys.* **55**, 572 (1971).
15. R. Abbel *et al.*, *J. Am. Chem. Soc.* **131**, 833 (2009).
16. S. A. Schmid *et al.*, *J. Am. Chem. Soc.* **131**, 17696 (2009).
17. H. Kautz, D. J. M. van Beek, R. P. Sijbesma, E. W. Meijer, *Macromolecules* **39**, 4265 (2006).
18. P. Cordier, F. Tournilhac, C. Soulié-Ziakovic, L. Leibler, *Nature* **451**, 977 (2008).
19. M. Burnworth *et al.*, *Nature* **472**, 334 (2011).
20. J. D. Hartgerink, E. Beniash, S. I. Stupp, *Science* **294**, 1684 (2001).
21. J. D. Hartgerink, E. Beniash, S. I. Stupp, *Proc. Natl. Acad. Sci. U.S.A.* **99**, 5133 (2002).
22. V. M. Tysseling-Mattiace *et al.*, *J. Neurosci.* **28**, 3814 (2008).
23. K. Rajangam *et al.*, *Nano Lett.* **6**, 2086 (2006).
24. A. Mata *et al.*, *Biomaterials* **31**, 6004 (2010).
25. R. N. Shah *et al.*, *Proc. Natl. Acad. Sci. U.S.A.* **107**, 3293 (2010).
26. E. D. Spoerke, S. G. Anthony, S. I. Stupp, *Adv. Mater.* **21**, 425 (2009).
27. H. W. Jun, V. Yuwono, S. E. Paramonov, J. D. Hartgerink, *Adv. Mater.* **17**, 2612 (2005).
28. G. A. Silva *et al.*, *Science* **303**, 1352 (2004).
29. D. A. Fletcher, R. D. Mullins, *Nature* **463**, 485 (2010).
30. H. G. Cui *et al.*, *Science* **327**, 555 (2010).
31. S. M. Zhang *et al.*, *Nat. Mater.* **9**, 594 (2010).
32. L. E. R. O'Leary, J. A. Fallas, E. L. Bakota, M. K. Kang, J. D. Hartgerink, *Nat. Chem.* **3**, 821 (2011).
33. R. M. Capito, H. S. Azevedo, Y. S. Velichko, A. Mata, S. I. Stupp, *Science* **319**, 1812 (2008).
34. D. I. Rożkiewicz, B. D. Myers, S. I. Stupp, *Angew. Chem. Int. Ed.* **50**, 6324 (2011).
35. A. P. H. J. Schenning, E. W. Meijer, *Chem. Commun.* **2005**, 3245 (2005).
36. L. C. Palmer, S. I. Stupp, *Acc. Chem. Res.* **41**, 1674 (2008).
37. F. S. Schoonbeek *et al.*, *Angew. Chem. Int. Ed.* **38**, 1393 (1999).
38. A. El-ghayoury, E. Peeters, A. P. H. J. Schenning, E. W. Meijer, *Chem. Commun.* **2000**, 1969 (2000).
39. A. Ajayaghosh, S. J. George, *J. Am. Chem. Soc.* **123**, 5148 (2001).
40. E. R. Zubarev, M. U. Pralle, E. D. Sone, S. I. Stupp, *J. Am. Chem. Soc.* **123**, 4105 (2001).
41. B. W. Messmore, J. F. Hulvat, E. D. Sone, S. I. Stupp, *J. Am. Chem. Soc.* **126**, 14452 (2004).
42. S. X. Xiao *et al.*, *J. Am. Chem. Soc.* **128**, 10700 (2006).
43. B. El Hamaoui *et al.*, *Chem. Commun.* **2007**, 2384 (2007).
44. J. S. Wu, W. Pisula, K. Müllen, *Chem. Rev.* **107**, 718 (2007).
45. J. P. Hill *et al.*, *Science* **304**, 1481 (2004).
46. Y. Yamamoto *et al.*, *Adv. Mater.* **18**, 1297 (2006).
47. W. Jin *et al.*, *J. Am. Chem. Soc.* **130**, 9434 (2008).
48. W. Jin *et al.*, *Proc. Natl. Acad. Sci. U.S.A.* **102**, 10801 (2005).
49. C. Didraga *et al.*, *J. Phys. Chem. B* **108**, 14976 (2004).
50. D. M. Eisele, J. Knoester, S. Kirstein, J. P. Rabe, D. A. Vanden Bout, *Nat. Nanotechnol.* **4**, 658 (2009).
51. A. P. H. J. Schenning *et al.*, *J. Am. Chem. Soc.* **124**, 10252 (2002).
52. E. H. A. Beckers *et al.*, *J. Am. Chem. Soc.* **128**, 649 (2006).
53. Y. Yamamoto *et al.*, *Science* **314**, 1761 (2006).
54. Y. Yamamoto *et al.*, *Proc. Natl. Acad. Sci. U.S.A.* **106**, 21051 (2009).
55. W. Zhang *et al.*, *Science* **334**, 340 (2011).
56. A. L. Sisson *et al.*, *Angew. Chem. Int. Ed.* **47**, 3727 (2008).
57. N. Sakai, R. Bhosale, D. Emery, J. Mareda, S. Matile, *J. Am. Chem. Soc.* **132**, 6923 (2010).
58. M. Sofos *et al.*, *Nat. Mater.* **8**, 68 (2009).
59. Q. Wang *et al.*, *Nature* **463**, 339 (2010).

Acknowledgments: Experimental work featured in this Review was supported by the Japan Science and Technology Agency and RIKEN (T.A.'s laboratory); the Dutch National Science Foundation NWO and ERC (E.W.M.'s laboratory); and the U.S. Department of Energy Basic Energy Sciences Program (grants DE–FG02-00ER45810 and EFRC Non-Equilibrium Research Center DE-SC0000989), the NIH (grants NIDCR: 2R01DE015920-06 and NIBIB: 2R01EB003806-06A2), and the NSF (grant DMR-1006713) (S.I.S.'s laboratory). We thank M. Seniw (Northwestern Univ.) for the preparation of figures and A. Tayi (Northwestern Univ.) and K. Pieterse (Eindhoven Univ. of Technology) for assistance with the preparation of the manuscript.

10.1126/science.1205962

the seawater from which their Li is derived. Secular variations in δ^7Li_{SW} must thus reflect imbalances between the sources and sinks of Li to and from the ocean, driven by perturbations in the global silicate weathering and reverse-weathering cycles (*14*, *15*).

Seawater lithium budget. The fluxes of river Li and HT Li to the sea are comparable in magnitude but isotopically very distinct. High-temperature HT vent fluids (>350°C) are highly enriched in Li above seawater ($[Li]_{HT} \approx 840$ μM) but are only slightly fractionated from their source rocks ($\delta^7Li_{HT} \approx 8.3‰$; $\delta^7Li_{MORB} \approx 3.7‰$). The ~4‰ enrichment of HT Li above MORB is probably because of ^6Li sequestration in HT Mg-rich greenstone alteration minerals (asbestos) during various stages of hydrothermal recirculation at mid-ocean ridges. In contrast, riverine Li ($\delta^7Li_{Riv} \approx 23‰$) is ~21‰ heavier than continental source rocks (upper continental crust; $\delta^7Li_{UCC} = 1.7‰$) (*3*, *4*, *16*, *17*) (figs. S2 to S5 and text S1).

Modern-day riverine dissolved Li displays a large spread in concentration and isotopes. Only about one-fifth of continentally weathered Li is carried in the dissolved load. The remainder is carried as Li in secondary clays (*2*, *6*) (fig. S3). The large isotopic offset (21‰) observed between δ^7Li_{Riv} and δ^7Li_{UCC} is a function of chemical weathering intensity (*18*, *19*). The preferential uptake of ^6Li into secondary aluminosilicate clay minerals and oxides formed during weathering and transport drives δ^7Li_{Riv} much heavier than the average continental crust. The partitioning of riverine Li into dissolved and secondary phases as a function of weathering intensity and weathering regimes determines both dissolved Li flux ($F_{Riv\text{-}Li}$) and δ^7Li_{Riv}. Peneplained terrains, especially those in the tropics with transport-limited regimes, exhibit congruent weathering, little or no secondary dioctahedral clay formation to entrap and transport cations, and hence dissolved Li isotope ratios that reflect their source silicate bedrocks. High-relief terrains (uplifted mountains and downcutting high plateaus) with weathering-limited regimes exhibit high physical and chemical weathering and denudation rates with extreme incongruent weathering, large rates of secondary clay formation that carry most of the weathered Li down rivers, and hence dissolved Li isotopes ratios that are ^7Li-enriched relative to their source rocks (*5*, *20*, *21*) (text S1).

At steady state, marine Li removal processes must balance the fluvial and hydrothermal inputs. We group the Li removal processes together and term them "reverse weathering" (*13*). Preferential removal of ^6Li into marine clays, similar to that on continents, leads to a large removal-induced fractionation. This reverse weathering–driven fractionation, representing "light" fractionation from the seawater Li source of about 16‰ ($\Delta_{SW\text{-}Sink} \approx 16‰$), drives seawater isotopically heavy (*11*, *12*) (text S1). Without this removal-induced Li isotope fractionation, seawater would simply reflect the flux-weighted isotope ratio of its sources ($\delta^7Li_{Input} \approx 15‰$). For a steady-state ocean, this removal-driven fractionation puts a boundary condition on composition of the input fluxes because δ^7Li_{SW} must remain about 16‰ heavier than δ^7Li_{Inputs}. This characteristic of Li isotopes in seawater with its large isotopic separation is unique.

The removal of Li by low-temperature reverse-weathering reactions includes MAAC formation in sediments (*22*) and low-temperature seafloor basalt alteration (AOC formation) (*7*, *8*, *16*), both of which involve formation of Mg-rich smectites (*9*–*11*), and Fe-rich aluminosilicates in muddy shallow-water sediments (*23*). Lithium is prone to substitute for octahedral Mg in both high-temperature and low-temperature "clays." Low-temperature weathering (<250°C) of ridge flank

Table 1. Best estimates of dissolved Li input and output fluxes and their compositions from published results (text S1).

Input/output	Lithium flux (10^9 moles/year)	Average δ^7Li (‰)	References
Inputs			
Rivers, F_{Riv}	10	23	(*2*, *5*, *6*)
Hydrothermal vents, F_{HT}	13	8.3	(*3*, *4*)
Subduction reflux, F_{Reflx}	6	15	(*10*, *26*, *27*)
Total input, F_{Input}	29	15	
Outputs			
Basalt alteration (AOC), F_{AOC}	8	15	(*7*, *8*, *17*, *26*)
Sediment uptake (MAAC), F_{MAAC}	20	15	(*9*, *10*, *14*, *26*, *27*)
$\Delta_{Seawater\text{–}Sediment}$ ($\delta^7Li_{SW} - \delta^7Li_{Sink}$)		16	(*10*, *11*)
Total reverse weathering, F_{Sink}	29	15	

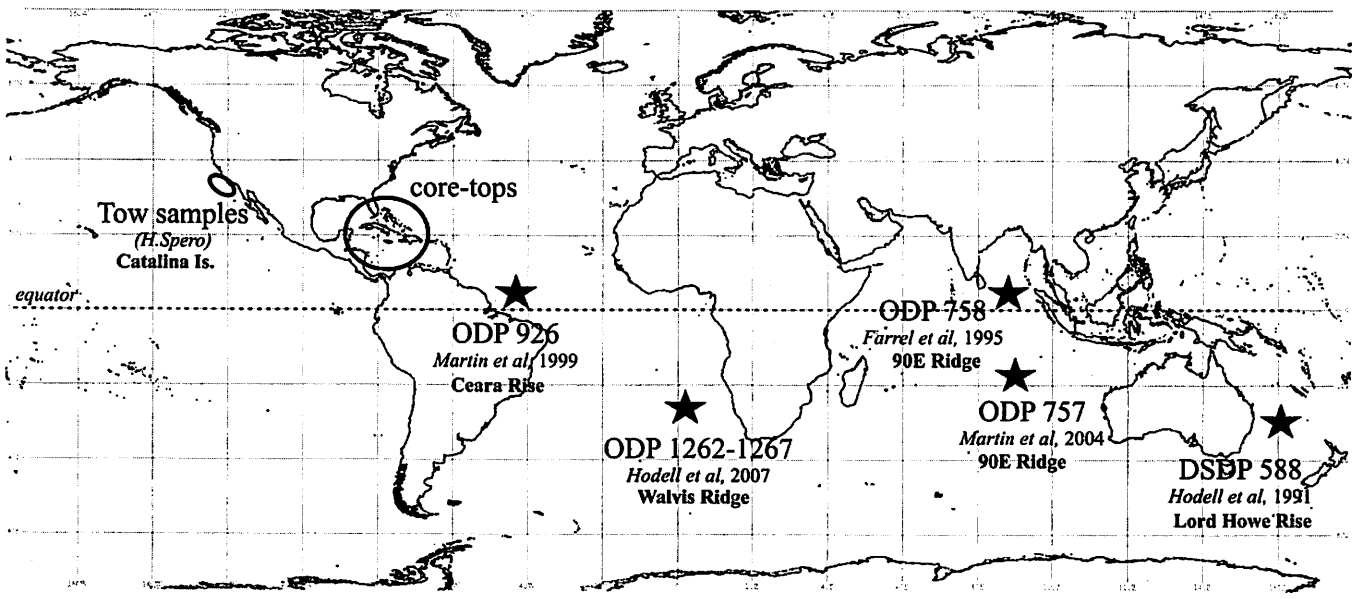

Fig. 2. DSDP/ODP drill sites 588, 757, 758, 926, 1262, 1263, 1265, and 1267, with preexisting high-resolution seawater strontium isotope records, from which the foraminifera samples for this work were collected (*25*) (text S2 and table S1).

basalts away from spreading centers acts as a net sink for Li. In many respects, Li is a crustally recycled cation (*4*, *8*, *9*), being sourced to the ocean from HT circulation at the ridge axis and then reconsumed into basalts during low-temperature alteration off axis. In today's ocean, MAAC is responsible for ~70% and AOC for ~30% of the total marine lithium removal by reverse weathering (Table 1).

Seawater lithium isotope record. Our seawater Li isotope record was constructed by analyzing chemically cleaned planktonic foraminifera that incorporate trace quantities of seawater dissolved Li into their calcium carbonate tests during growth in the surface ocean ($[Li^+]_{Foram} \approx 1$ to 2 ppm). This intrinsic lattice-bound Li isotope ratio is independent of temperature and Li concentration (*15*). The analytical challenges associated with precise δ^7Li determinations from mass-limited foraminifera samples (<1 mg) without contamination and laboratory fractionation artifacts were overcome by developing new methods (*24*, *25*). We have validated the application of foraminifera as faithful recorders of δ^7Li_{SW} (fig. S6) without significant diagenetic overprints (text S3). We selected eight Deep Sea Drilling Project (DSDP)–Ocean Drilling Program (ODP) sites with existing high-resolution Sr isotope records, minimal diagenesis, and good chronologies (Fig. 2). We analyzed age- and species-overlapping foraminifera samples (n = 301) at a resolution of 500,000 to 1 million years, which included both individual species and bulk foraminifera (Fig. 3).

We make six important assumptions for mass balance calculations that drive the observed changes in δ^7Li_{SW}: (i) In contrast to previous δ^7Li_{SW} mass balance studies (*7*, *15*), we include a Li "subduction reflux" term that recognizes solutions resulting from dewatering and breakdown of MAAC in the downgoing slab during subduction and expulsed via the decollement back to the ocean (*26*, *27*) (Table 1 and text S1). This subduction reflux of Li from the convergent margins is held constant over time at ~6×10^9 moles of Li per year (the present-day value), and its isotopic composition is set at a constant offset from contemporaneous seawater ($\delta^7Li_{Reflx} = \delta^7Li_{SW} - \delta^7Li_{Sink}$). This estimate of subduction reflux terms is based on instantaneous steady-state balances, whereas on the real Earth there is a time delay of 50 to 100 million years between sediment deposition and crustal subduction. However, this flux of Li from MAAC and AOC breakdown has a minor influence on seawater Li mass and isotope budgets. (ii) Initially, for simplicity, we take the fluvial dissolved $F_{Riv\text{-}Li}$ as constant over the Cenozoic (this constraint is later dropped). Nevertheless, from the early Paleogene to the present, the river-borne total weathered Li flux (suspended + dissolved) has increased by ~300% as a result of increased orogeny. More important, increasingly incongruent chemical weathering of the continents has changed the dominant Li-bearing phase in rivers from dissolved Li in the Paleocene to suspended Li (in clays) today. This weathering-driven redistribution of riverine Li flux has changed the ratio of dissolved to suspended partitioning from 4:1 in Paleocene to 1:4 today. (iii) δ^7Li_{HT} is kept at the modern-day value of 8.3‰. (iv) $F_{HT\text{-}Li}$ is kept constant over the Cenozoic (*28*). (v) Fractionation of Li upon removal from seawater during reverse weathering ($\Delta_{SW\text{-}SED} = \delta^7Li_{SW} - \delta^7Li_{Sink} \approx 16‰$) is kept constant because the processes of Li removal, whether sediment-hosted or by alteration of oceanic crust, likely has not changed over the Cenozoic. (vi) The removal flux of Li out of the ocean (F_{Sink}) has remained near steady state with the inputs and exhibits first-order removal kinetics with respect to the Li concentration of seawater (Li_{SW}). Our interpretation of changes in δ^7Li_{SW} is based on the weathering and reverse-weathering processes that have the largest δ^7Li fractionation factors and thus the highest likelihood to be the main drivers not only of ocean δ^7Li_{SW} change but also other changes in oceanic and atmospheric chemistry and climate driven by silicate weathering (*29*, *30*) (text S4).

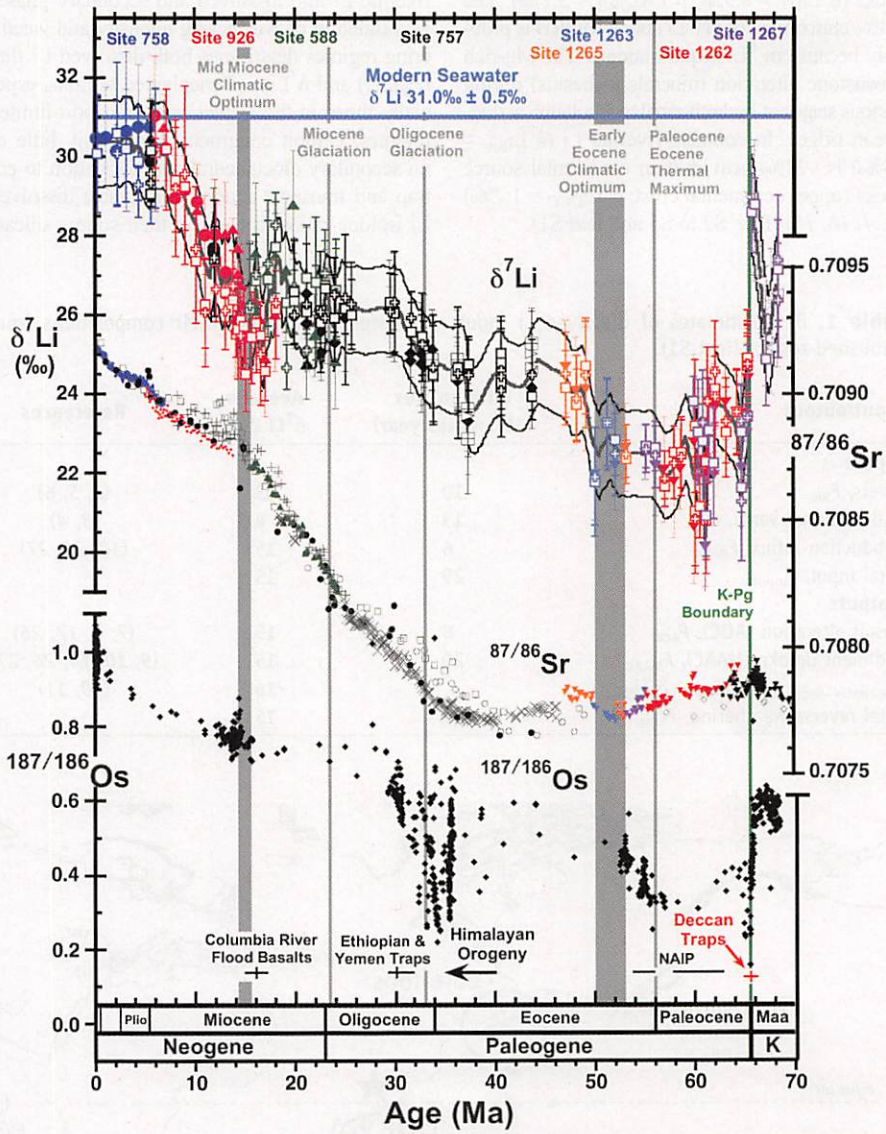

Fig. 3. Late Cretaceous to Holocene Li isotope record (covering 68 million years) and published values of seawater records for $^{87}Sr/^{86}Sr$ and $^{187}Os/^{186}Os$. Lithium isotope values (δ^7Li), expressed as per mil (‰) variation from NIST L-SVEC standard (SRM 8545) (*25*), are plotted on the top left y axis. The error bars represent 2σ uncertainty associated with each quintuplicate measurement. The gray line represents 5-point running mean of δ^7Li_{Foram} record; the two parallel black lines are the corresponding ±2σ uncertainty based on the average SD of all δ^7Li_{Foram} measurements (σ = ±0.55‰, n = 301). The individual foraminifera species symbols are listed in fig. S8. Foraminiferal Li and Sr data are color-coded according to drill sites and are plotted on the same age chronology (*33*, *50*–*53*). The Cretaceous-Tertiary (K-Pg) boundary is set at 65.68 Ma (*54*). The Cenozoic marine Os isotope record ($^{187}Os/^{186}Os$) is plotted on the bottom left y axis (*34*, *35*) (text S2). Because of osmium's short residence time in the ocean and its isotopic sensitivity to impacts and mantle sources (LIPs), the $^{187}Os/^{186}Os$ record reflects large abrupt shifts that are not discernable in either the $^{87}Sr/^{86}Sr$ or $^7Li/^6Li$ records.

Our seawater Li isotope record is consistent with previous Neogene reconstructions from chemically cleaned planktonic foraminifera (*15*, *31*) (fig. S7). Also, our two paleo-δ^7Li_{SW} records from individual species and from bulk foraminifera are indistinguishable from one another (fig. S8). This similarity implies an absence of biogenic fractionation (vital effects) in δ^7Li_{SW} recorded by different species of foraminifera (both extant and extinct), despite strong discrimination against Li by foraminifera [lithium distribution coefficient $K^D_{Li(Calcite-Seawater)} = (Li/Ca)_{Calcite}/(Li/Ca)_{Seawater} \approx 4.2 \times 10^{-3}$ mol/mol] and large variations in observed $(Li/Ca)_{Foram}$ (fig. S6). Also, fossil foraminifera from different drill sites at different paleolatitudes and paleodepths and under markedly different calcite preservation states display no offset or memory effects or diagenetic resetting (text S3 and fig. S9). The absence of any systematic differences in foraminifera-based δ^7Li_{SW} values between samples for both individual species and bulk foraminifera samples of the same age from different drill sites demonstrates that within the resolution of the present record, dissolved Li in seawater was isotopically homogeneous, and cleaned bulk foraminifera can be used to reconstruct the long-term evolution of δ^7Li_{SW}. Our modern foraminifera δ^7Li_{SW} appear to average ~1‰ lighter than seawater (fig. S6).

Results and interpretations. Our paleo-δ^7Li_{SW} record exhibits a 9‰ rise during the past 60 million years, implying a shift in chemical weathering of continental rocks consistent with the seawater $^{87}Sr/^{86}Sr$ record (Fig. 3). The isotope record shows no change over the past 6 million years; thus, the Li content and δ^7Li_{SW} of modern seawater are presumed to be near steady state (Fig. 1). Although our Li isotope record is similar to the seawater Sr isotope history, the Cenozoic δ^7Li_{SW} does not exhibit the monotonically increasing trend of seawater $^{87}Sr/^{86}Sr$. The rise in δ^7Li_{SW} during the Cenozoic is nonlinear, punctuated by transient flat steady states and quasi-linear rises that may coincide with major climatic and tectonic events (*32*). The history of δ^7Li_{SW} over the past 60 million years can be divided into periods of stepped rises (Fig. 4). From 52 to 47 million years ago (Ma), 35 to 31 Ma, and 14 to 6 Ma, the average rate of increase in δ^7Li_{SW} ($\Delta\delta^7Li_{SW} / \Delta t$) is ~ 0.4‰ ± 0.1‰ per million years (2σ). The net result is a 9‰ rise in δ^7Li_{SW} during the past 60 million years. We argue that this increase in δ^7Li_{SW} is caused primarily by increases in δ^7Li_{Riv} (text S4 and fig. S10) that drive increases in the isotopic value entering the sea. Within several residence times (several million years), the marine reverse-weathering removal sink must adjust to obtain a new balance. The mechanism for this clay formation feedback is likely linked to the aluminum source from the continents (clays) and changes in the lithium and magnesium concentrations of seawater (Li_{SW}/Mg_{SW}).

Seawater $^{87}Sr/^{86}Sr$ and $^{187}Os/^{188}Os$ are dependent on differences in isotopic compositions (no isotope fractionation) in their continental (radiogenic) and mantle (nonradiogenic) sources to the ocean (Fig. 3) (*32*–*35*). However, weathering of continental carbonates and redissolution of marine carbonates (for Sr) and weathering of organic-rich black shales and the rain of cosmic dust (for Os) complicate the uplift and continental runoff connections because these elements are not hosted solely in silicates, in contrast to Li (*2*, *36*, *37*). Increased silicate weathering during the Cenozoic has also been suggested from the records of seawater $\delta^{44/40}Ca$ (*38*) and Sr/Ca (*39*), but both suffer from nonsilicate sources and sinks. The sulfur isotope history of seawater (*40*), an ocean redox record of S burial in marine sediments, suggests an oceanic anoxic event near the Paleocene-Eocene Thermal Maximum best explained as an increase in sediment sulfide burial, but is mute on changes in tectonics and weathering. Lithium is unique in tagging processes involving silicates, which is the key to carbon dioxide consumption during weathering and thus the connection between uplift tectonics and climate (*15*, *29*, *41*, *42*).

The Paleocene-Eocene δ^7Li_{SW} minimum. Isotope and mass balance estimates for the mid-Paleocene δ^7Li_{SW} minimum (~22‰), based on our understanding of the modern-day oceanic Li cycle (Fig. 1B), predict an extremely light δ^7Li_{Riv} (~2 to 6‰) reflecting near-congruent weathering of the UCC regardless of secular changes in the Li river flux (text S4 and fig. S10). The early Cenozoic hothouse climate—with high sea levels,

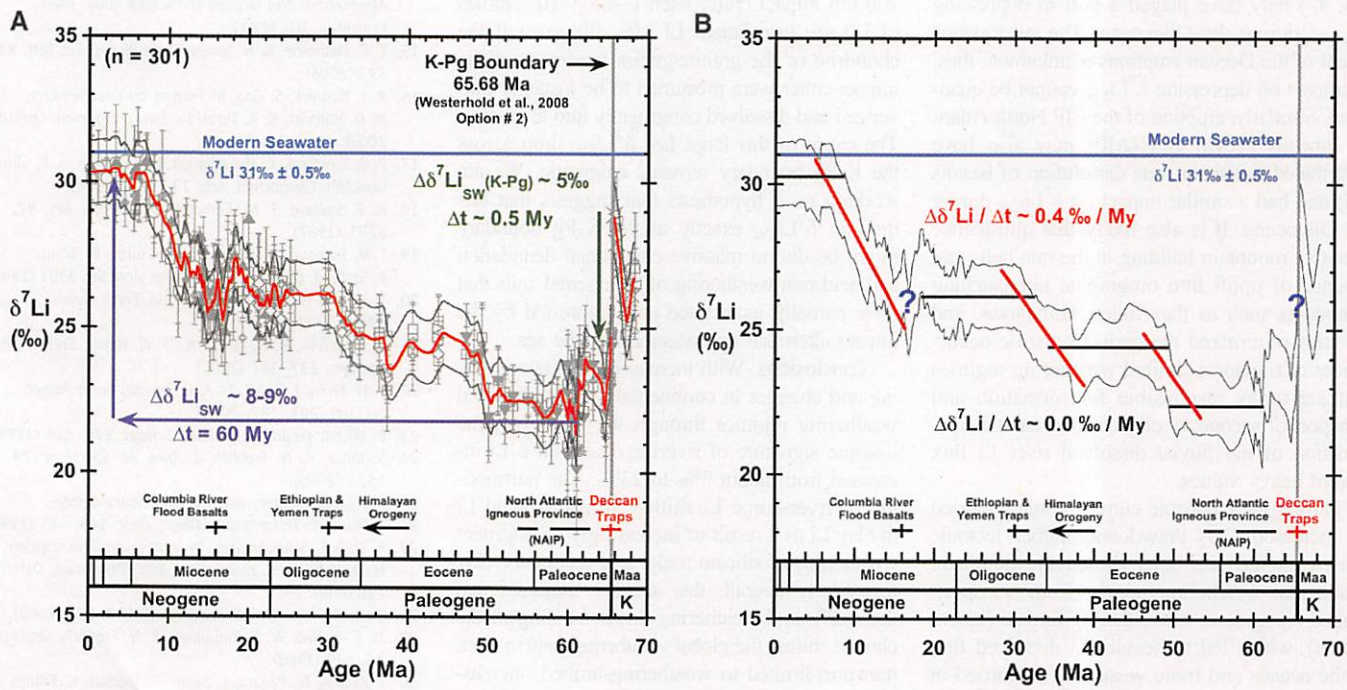

Fig. 4. (**A**) The 5-point running mean of all δ^7Li_{Foram} values from all foraminiferal Li isotope ratio analyses (red line) plotted according to their average age with 2σ uncertainty (the two parallel gray lines) (Fig. 3). The vertical green downward arrow marks the rapid drop in δ^7Li across the K-Pg boundary. The horizontal and vertical purple arrows reflect the overall 9‰ rise in δ^7Li_{SW} during the Cenozoic. (**B**) The ~9‰ rise in δ^7Li_{Foram} over the last 60 million years has been divided into four distinct periods of steady state (black horizontal lines, $\Delta\delta^7Li/\Delta t \approx 0.0$‰ per million years) and three periods of rapid increase in δ^7Li_{SW} (red lines, $\Delta\delta^7Li/\Delta t \approx 0.4$‰ per million years).

swamp continents, and cation-depleted peneplained continents dominated by neotropical congruent weathering and high weathering intensity under hot rainy conditions—is consistent with this interpretation. Low-latitude rivers during this period probably carried sparse suspended material or secondary clays. Thus, the cations delivered to the ocean were mostly in the dissolved load. The implication is that over the Cenozoic the proportion of dissolved Li flux to the ocean decreased (while clay Li increased) and its isotopic value (δ^7Li_{Riv}) increased as the chemical weathering regime of the continents became more weathering limited because of tectonic uplift in the rain belts (e.g., the Himalayas). The interpretation of the Mg/Ca change in seawater, which implies a slowdown in HT fluxes with time, is not inconsistent with the direction of change of our Li isotope record, but the magnitude of HT changes required seems unreasonable (text S4).

The δ^7Li_{SW} minimum in the early Cenozoic may have also been influenced by the northward migration of India carrying the recently erupted Large Igneous Province (LIP) Deccan Traps across the equatorial rain belt (*43*, *44*). LIPs probably have a Li concentration and δ^7Li composition similar to MORB (6 ppm; 3.7‰). Because basalts are aluminum-deficient relative to granites, they weather very rapidly (*45*) and highly congruently (few secondary cation-bearing clays to fractionate Li isotopes) (*12*). Thus rapid chemical dissolution of the Deccan basalts during the 10-million-year equatorial passage in a geological period of much more intense equatorial rainfall (*46*, *47*) may have played a part in depressing δ^7Li_{SW} during the Oligocene. The subaqueous extent of the Deccan eruptions is unknown; thus, its impact on depressing δ^7Li_{SW} cannot be quantified. Similarly, eruption of the LIP North Atlantic Igneous Provinces (NAIP) may also have contributed to subaqueous dissolution of basalts (*45*) and had a similar impact on δ^7Li_{SW} during the Oligocene. It is also likely that quiescence of active mountain building in the rain belts and absence of uplift into orographic rain-catching mountains such as the Andes, Himalayas, and Rockies minimized the early Cenozoic occurrences of transport-limited weathering regimes that are today responsible for formation and transport of secondary clays to the sea and fractionation of the fluvial dissolved river Li flux toward heavy values.

During the Cenozoic climate cooling caused by increased CO_2 drawdown, higher tectonic activity in the rain belts shifted the dominant continental weathering regime from transport-limited (congruent) to weathering-limited (incongruent), which led to heavier Li dissolved flux to the oceans and more weathered Li carried in clays (*14*). Thus, the similarity of our δ^7Li_{SW} record with the global ocean bottom water $\delta^{18}O$ (temperature and ice volume) record is perhaps not accidental (fig. S11). This interpretation suggests that the rises in δ^7Li_{SW} punctuated with stable plateaus every 10 million years or so since the late Eocene might reflect periods of active uplift and denudation followed by periods of tectonic inactivity, at least in the low-latitude rain belts where most continental chemical weathering is expected to occur (Fig. 3). This scenario of Cenozoic continental silicate weathering is different from a monotonically increasing continental chemical weathering regime after initiation of the Himalayan uplift as suggested by the seawater Sr isotope history (*32*, *33*). Coupled Sr and Li isotope models may lead to a better understanding of secular changes in chemical weathering of continental silicates and carbonates and the importance of cation-bearing clay fluxes to the sea in the CO_2-consumption term of climate models (*41*).

The Cretaceous-Paleogene boundary (KTB) δ^7Li_{SW} event. An abrupt 5‰ drop in δ^7Li_{SW} occurs in less than 500,000 years across the Cretaceous-Paleogene (Tertiary) boundary (K-Pg or KTB), simultaneous with the seawater iridium and osmium isotope spikes (Fig. 3) (*44*). This rapid drop in δ^7Li_{SW} must be due to a large instantaneous delivery of isotopically light Li to the sea comparable to the Li content of the entire Cretaceous ocean. It is probably not due to fast addition of Li to seawater from congruent weathering of freshly erupted Deccan Traps ($\delta^7Li_{Basalt} \approx 3.7‰$) (*43*). Given the inventory of Li in seawater today (~3.4×10^{16} moles) and the possibility that this may have been higher in the Cretaceous, the Li mass of the Chicxulub bolide (~10 km diameter; ~9×10^{11} moles of Li) carrying chondritic δ^7Li (~2‰) or even the 200-km impact crater itself (~4.5×10^{14} moles of Li) are insufficient Li (*48*, *49*), even if the chondrite or the granite/gneiss basement of the impact crater were presumed to be instantly pulverized and dissolved congruently into the ocean. The cause of this large fast δ^7Li_{SW} drop across the K-Pg boundary remains enigmatic. We are working on a hypothesis that suggests that this drop in δ^7Li_{SW} exactly at the K-Pg boundary might be due to massive continental denudation and acid rain weathering of continental soils that were partially incinerated and deforested by the impact aftermath and washed into the sea.

Conclusions. With increased mountain building and changes in continental silicate chemical weathering regimes through the Cenozoic, the isotopic signature of riverine dissolved δ^7Li increased from about 3‰ to 23‰. The partitioning of river-borne Li shifted from dissolved Li to clay Li as a result of increasingly incongruent weathering of silicate rocks and secondary clay formation. Overall, this scenario requires that the uplift- and weathering-driven cooling of the climate shifted the global weathering pattern from transport-limited to weathering-limited, increasing secondary clay mineral formation during weathering. As a result of preferential retention of ^6Li by secondary clays, the δ^7Li of river-borne Li became progressively heavier, driving seawater to its present heavy value. An increase in total Li weathered and delivered to the sea (clay Li plus dissolved Li), if extended to the weathering intensity of the major igneous cations stored in the sea (Na, K, and Mg), suggests faster CO_2 drawdown due to more rapid weathering rates. Direct quantification of the influences of forward chemical weathering of continental silicate rocks and reverse weathering of marine silicates on δ^7Li_{SW} might provide alternative estimates of atmospheric CO_2 consumption by the silicate weathering and reverse-weathering cycles (*42*).

References and Notes

1. W. S. Broecker, T. Peng, *Tracers in the Sea* (Lamont-Doherty Geological Observatory, Columbia University, 1982).
2. M. R. Palmer, J. M. Edmond, *Geochim. Cosmochim. Acta* **56**, 2099 (1992).
3. L. H. Chan *et al.*, *Geochim. Cosmochim. Acta* **58**, 4443 (1994).
4. H. Elderfield, A. Schultz, *Annu. Rev. Earth Planet. Sci.* **24**, 191 (1996).
5. Y. Huh, L.-H. Chan, L. Zhang, J. M. Edmond, *Geochim. Cosmochim. Acta* **62**, 2039 (1998).
6. J. Gaillardet, J. Viers, B. Dupré, in *Treatise on Geochemistry*, H. D. Holland, K. K. Turekian, Eds. (Pergamon, Oxford, 2003), pp. 225–272.
7. W. E. Seyfried Jr., X. Chen, L. H. Chan, *Geochim. Cosmochim. Acta* **62**, 949 (1998).
8. L. H. Chan, J. Edmond, G. Thompson, K. Gillis, *Earth Planet. Sci. Lett.* **108**, 151 (1992).
9. L. H. Chan, W. P. Leeman, T. Plank, *Geochem. Geophys. Geosyst.* **7**, Q06005 (2006).
10. R. H. James, M. D. Rudnicki, M. R. Palmer, *Earth Planet. Sci. Lett.* **171**, 157 (1999).
11. N. Vigier *et al.*, *Geochim. Cosmochim. Acta* **72**, 780 (2008).
12. A. Verney-Carron, N. Vigier, R. Millot, *Geochim. Cosmochim. Acta* **75**, 3452 (2011).
13. F. T. Mackenzie, R. M. Garrels, *Am. J. Sci.* **264**, 507 (1966).
14. H. D. Holland, *The Chemical Evolution of the Atmosphere and Oceans* (Princeton Univ. Press, Princeton, NJ, 1984).
15. E. C. Hathorne, R. H. James, *Earth Planet. Sci. Lett.* **246**, 393 (2006).
16. R. L. Rudnick, S. Gao, in *Treatise on Geochemistry*, H. D. Holland, K. K. Turekian, Eds. (Pergamon, Oxford, 2003), pp. 1–64.
17. P. B. Tomascak, C. H. Langmuir, P. J. Le Roux, S. B. Shirey, *Geochim. Cosmochim. Acta* **72**, 1626 (2008).
18. R. F. Stallard, J. M. Edmond, *J. Geophys. Res.* **92**, 8293 (1987).
19. J. M. Edmond, M. Palmer, C. Measures, B. Grant, R. Stallard, *Geochim. Cosmochim. Acta* **59**, 3301 (1995).
20. Y. Huh, L. H. Chan, J. M. Edmond, *Earth Planet. Sci. Lett.* **194**, 189 (2001).
21. B. Kisakűrek, R. H. James, N. B. W. Harris, *Earth Planet. Sci. Lett.* **237**, 387 (2005).
22. L. H. Chan, J. C. Alt, D. A. H. Teagle, *Earth Planet. Sci. Lett.* **201**, 187 (2002).
23. P. Michalopoulos, R. C. Aller, *Science* **270**, 614 (1995).
24. S. Misra, P. N. Froelich, *J. Anal. At. Spectrom.* **24**, 1524 (2009).
25. See supplementary material on *Science* Online.
26. T. Plank, C. H. Langmuir, *Chem. Geol.* **145**, 325 (1998).
27. Y. Li, J. E. Schoonmaker, in *Treatise on Geochemistry*, H. D. Holland, K. K. Turekian, Eds. (Pergamon, Oxford, 2003), pp. 1–35.
28. D. B. Rowley, *Geol. Soc. Am. Bull.* **114**, 927 (2002).
29. M. E. Raymo, W. F. Ruddiman, P. N. Froelich, *Geology* **16**, 649 (1988).
30. J. Zachos, M. Pagani, L. Sloan, E. Thomas, K. Billups, *Science* **292**, 686 (2001).
31. J. M. Hall, L.-H. Chan, W. F. McDonough, K. K. Turekian, *Mar. Geol.* **217**, 255 (2005).
32. J. Hess, M. L. Bender, J. G. Schilling, *Science* **231**, 979 (1986).
33. D. A. Hodell, P. A. Mueller, J. R. Garrido, *Geology* **19**, 24 (1991).

34. B. Peucker-Ehrenbrink, G. Ravizza, *Terra Nova* **12**, 205 (2000).
35. B. Peucker-Ehrenbrink, G. Ravizza, in *The Geologic Time Scale*, F. M. Gradstein, J. G. Ogg, M. D. Schmitz, Eds. (Cambridge Univ. Press, Cambridge, 2012), chapter 8; 10.1016/B978-0-444-59425-9.00008-1.
36. J. M. Edmond, *Science* **258**, 1594 (1992).
37. B. Peucker-Ehrenbrink, R. E. Hannigan, *Geology* **28**, 475 (2000).
38. E. M. Griffith, A. Paytan, K. Caldeira, T. D. Bullen, E. Thomas, *Science* **322**, 1671 (2008).
39. C. H. Lear, H. Elderfield, P. A. Wilson, *Earth Planet. Sci. Lett.* **208**, 69 (2003).
40. A. Paytan, M. Kastner, D. Campbell, M. H. Thiemens, *Science* **304**, 1663 (2004).
41. R. A. Berner, A. C. Lasaga, R. M. Garrels, *Am. J. Sci.* **283**, 641 (1983).
42. F. T. Mackenzie, L. R. Kump, *Science* **270**, 586 (1995).
43. V. Courtillot, P. R. Renne, *C. R. Geosci.* **335**, 1 (2003).
44. D. V. Kent, G. Muttoni, *Proc. Natl. Acad. Sci. U.S.A.* **105**, 16065 (2008).
45. S. R. Gislason, E. H. Oelkers, A. Snorrason, *Geology* **34**, 49 (2006).
46. C. Jaramillo, M. J. Rueda, G. Mora, *Science* **311**, 1893 (2006).
47. M. T. Clementz, J. O. Sewall, *Science* **332**, 455 (2011).
48. L. W. Alvarez, W. Alvarez, F. Asaro, H. V. Michel, *Science* **208**, 1095 (1980).
49. P. Schulte *et al.*, *Science* **327**, 1214 (2010).
50. J. W. Farrell, S. C. Clemens, L. Peter Gromet, *Geology* **23**, 403 (1995).
51. E. E. Martin, H. D. Scher, *Earth Planet. Sci. Lett.* **220**, 25 (2004).
52. E. E. Martin, N. J. Shackleton, J. C. Zachos, B. P. Flower, *Paleoceanography* **14**, 74 (1999).
53. D. A. Hodell *et al.*, *Geochem. Geophys. Geosyst.* **8**, Q09001 (2007).
54. T. Westerhold *et al.*, *Palaeogeogr. Palaeoclimatol. Palaeoecol.* **257**, 377 (2008).

Acknowledgments: We thank the U.S. National Science Foundation (MG&G), American Chemical Society (Petroleum Research Fund), and The Francis Eppes Society of Florida State University for providing financial support. We sincerely thank S. Clemens, D. Hodell, E. Hathorne, E. Martin, E. Thomas, W. Landing, and H. Spero for providing samples. The manuscript greatly benefited from the constructive reviews of M. Bender, V. Salters, M. Humayun, A. Paytan, P. Pogge von Strandmann, and an anonymous reviewer. We are very thankful to B. Peucker-Ehrenrbrink and G. Ravizza for providing the osmium isotope data from GTS 2012 (in press). We also thank H. Elderfield, I. N. McCave, and A. Galy for helpful discussions. Tabulated data are provided on *Science* Online.

Supporting Online Material

www.sciencemag.org/cgi/content/full/science.1214697/DC1
Materials and Methods
SOM Text
Figs. S1 to S11
Table S1
References (*55–157*)

30 September 2011; accepted 17 January 2012
Published online 26 January 2012;
10.1126/science.1214697

A Systematic Survey of Loss-of-Function Variants in Human Protein-Coding Genes

Daniel G. MacArthur,[1,2*] Suganthi Balasubramanian,[3,4] Adam Frankish,[1] Ni Huang,[1] James Morris,[1] Klaudia Walter,[1] Luke Jostins,[1] Lukas Habegger,[3,4] Joseph K. Pickrell,[5] Stephen B. Montgomery,[6,7] Cornelis A. Albers,[1,8] Zhengdong D. Zhang,[9] Donald F. Conrad,[10] Gerton Lunter,[11] Hancheng Zheng,[12] Qasim Ayub,[1] Mark A. DePristo,[13] Eric Banks,[13] Min Hu,[1] Robert E. Handsaker,[13,14] Jeffrey A. Rosenfeld,[15] Menachem Fromer,[13] Mike Jin,[3] Xinmeng Jasmine Mu,[3,4] Ekta Khurana,[3,4] Kai Ye,[16] Mike Kay,[1] Gary Ian Saunders,[1] Marie-Marthe Suner,[1] Toby Hunt,[1] If H. A. Barnes,[1] Clara Amid,[1,17] Denise R. Carvalho-Silva,[1] Alexandra H. Bignell,[1] Catherine Snow,[1] Bryndis Yngvadottir,[1] Suzannah Bumpstead,[1] David N. Cooper,[18] Yali Xue,[1] Irene Gallego Romero,[1,5] 1000 Genomes Project Consortium, Jun Wang,[12] Yingrui Li,[12] Richard A. Gibbs,[19] Steven A. McCarroll,[13,14] Emmanouil T. Dermitzakis,[7] Jonathan K. Pritchard,[5,20] Jeffrey C. Barrett,[1] Jennifer Harrow,[1] Matthew E. Hurles,[1] Mark B. Gerstein,[3,4,21]† Chris Tyler-Smith[1]†

Genome-sequencing studies indicate that all humans carry many genetic variants predicted to cause loss of function (LoF) of protein-coding genes, suggesting unexpected redundancy in the human genome. Here we apply stringent filters to 2951 putative LoF variants obtained from 185 human genomes to determine their true prevalence and properties. We estimate that human genomes typically contain ~100 genuine LoF variants with ~20 genes completely inactivated. We identify rare and likely deleterious LoF alleles, including 26 known and 21 predicted severe disease–causing variants, as well as common LoF variants in nonessential genes. We describe functional and evolutionary differences between LoF-tolerant and recessive disease genes and a method for using these differences to prioritize candidate genes found in clinical sequencing studies.

Genetic variants predicted to severely disrupt protein-coding genes, collectively known as loss-of-function (LoF) variants, are of considerable scientific and clinical interest. Traditionally, such variants have been regarded as rare and having a high probability of being deleterious, on the basis of their well-established causal roles in severe Mendelian diseases such as cystic fibrosis and Duchenne muscular dystrophy. However, recent studies examining the complete genomes of apparently healthy subjects have suggested that such individuals carry at least 200 (*1*, *2*) and perhaps as many as 800 (*3*) predicted LoF variants. These numbers imply a previously unappreciated robustness of the human genome to gene-disrupting mutations and have important implications for the clinical interpretation of human genome–sequencing data.

Comparison of reported LoF variants between published genomes is complicated by differences in sequencing technology, variant-calling algorithms, and gene annotation sets between studies (*4*, *5*), and by the expectation that LoF variants will be highly enriched for false positives. The basis for this predicted enrichment is that strong negative natural selection is expected to act against the majority of variants inactivating protein-coding genes, thereby reducing the amount of true variation at these sites relative to the genome average, whereas sequencing error is expected to be approximately uniformly distributed; as a result, highly functionally constrained sites should show lower levels of observed polymorphism and substantially higher false-positive rates (*4*). To date, no large-scale attempt has been made to validate the LoF variants reported in published human genome sequences.

LoF variants found in healthy individuals will fall into several overlapping categories: severe recessive disease alleles in the heterozygous state; alleles that are less deleterious but nonetheless have an impact on phenotype and disease risk; benign LoF variation in redundant genes; genuine variants that do not seriously disrupt gene function; and, finally, a wide variety of sequencing

[1]Wellcome Trust Sanger Institute, Hinxton CB10 1SA, UK. [2]Discipline of Paediatrics and Child Health, University of Sydney, Sydney, NSW 2006, Australia. [3]Program in Computational Biology and Bioinformatics, Yale University, New Haven, CT 06520, USA. [4]Department of Molecular Biophysics and Biochemistry, Yale University, New Haven, CT 06520, USA. [5]Department of Human Genetics, University of Chicago, Chicago, IL 60637, USA. [6]Departments of Pathology and Genetics, Stanford University, Stanford, CA 94305–5324, USA. [7]Department of Genetic Medicine and Development, University of Geneva Medical School, 1211 Geneva 4, Switzerland. [8]Department of Haematology, University of Cambridge and NHS Blood and Transplant, Cambridge CB2 0PT, UK. [9]Department of Genetics, Albert Einstein College of Medicine, Bronx, NY 10461, USA. [10]Department of Genetics, Washington University School of Medicine, Saint Louis, MO 63110, USA. [11]Wellcome Trust Centre for Human Genetics, University of Oxford, Oxford OX3 7BN, UK. [12]BGI-Shenzhen, Shenzhen 518083, China. [13]Program in Medical and Population Genetics, Broad Institute of Harvard and MIT, Cambridge, MA 02142, USA. [14]Department of Genetics, Harvard Medical School, Boston, MA 02115, USA. [15]IST/High Performance and Research Computing, University of Medicine and Dentistry of New Jersey, Newark, NJ 07103, USA. [16]Molecular Epidemiology Section, Leiden University Medical Center, 2300 RC Leiden, Netherlands. [17]The European Nucleotide Archive, European Molecular Biology Laboratory–European Bioinformatics Institute, Hinxton CB10 1SD, UK. [18]Institute of Medical Genetics, School of Medicine, Cardiff University, Heath Park, Cardiff CF14 4XN, UK. [19]Human Genome Sequencing Center, Baylor College of Medicine, Houston, TX 77030, USA. [20]Howard Hughes Medical Institute, University of Chicago, Chicago, IL 60637, USA. [21]Department of Computer Science, Yale University, New Haven, CT, USA.

*To whom correspondence should be addressed. E-mail: macarthur@atgu.mgh.harvard.edu
†These authors contributed equally to this work.

and annotation artifacts. Distinguishing between these categories will be crucial for the complete functional interpretation of human genome sequences.

Obtaining and filtering candidate LoF variants. We identified 2951 candidate LoF variants using whole-genome sequencing data from 185 individuals analyzed as part of the pilot phase of the 1000 Genomes Project (*2*), as well as detailed analysis of high-coverage whole-genome sequencing data from a single anonymous European individual (*6*). The individuals represented three population groups: Yoruba individuals from Ibadan, Nigeria (YRI); 60 individuals of Northern and Western European origin from Utah (CEU); and 30 Chinese individuals from Beijing and 30 Japanese individuals from Tokyo who were analyzed jointly (CHB+JPT).

We adopted a definition for LoF variants expected to correlate with complete loss of function of the affected transcripts: stop codon–introducing (nonsense) or splice site–disrupting single-nucleotide variants (SNVs), insertion/deletion (indel) variants predicted to disrupt a transcript's reading frame, or larger deletions removing either the first exon or more than 50% of the protein-coding sequence of the affected transcript. We further subdivided these variants into "full" LoF variants predicted to affect all known protein-coding transcripts of the affected gene and "partial" variants affecting only a fraction of known coding transcripts. All annotation was performed against the Gencode v3b annotation (*7*) with the algorithm VAT (*8*).

We then subjected our candidate list to a series of stringent informatic and experimental validation steps (*9*). Informatic filtering was based on local sequence context (such as the presence of highly repetitive sequence), gene annotation (such as variants affecting noncanonical splice sites or located close to the end of the affected open reading frame), analysis of the effects of nearby variants (such as neighboring SNVs altering the predicted functional effect of the candidate LoF variant), and measures of sequence read mapping and quality (fig. S1). Where possible, thresholds for filtering were derived from the experimental validation experiments below.

We validated all candidate LoF SNVs and indels that were not excluded by other filters and for which we could design assays ($n = 1877$) with experimental genotyping using three Illumina genotyping arrays and 819 custom Sequenom assays run, where possible, on all 185 samples from the low- and high-coverage 1000 Genomes pilot projects. Large deletions had previously been subjected to extensive validation (*10*). All LoF variants identified in NA12878 were assessed by comparison with independent 454 sequencing and array-based data from the same individual, as well as targeted capillary sequencing of variants in highly repetitive regions. Finally, 786 variants were reexamined by complete manual reannotation of the 689 affected gene models by experienced curators, using the HAVANA annotation pipeline (*7*), to identify annotation errors and flag variants unlikely to profoundly affect gene function. All 589 candidate LoF variants identified in NA12878 were subjected to independent genotype validation and complete gene model reannotation.

As expected, the proportion of likely sequencing and annotation errors in the initial candidate set was high, with overlapping sets of 25.0, 26.8, and 11.1% examined LoF variants being excluded as representing likely sequencing or mapping errors, annotation or reference sequence errors, and variants unlikely to cause genuine LoF, respectively. Candidate LoF variants removed by filtering tended to be more common than high-confidence variants (Fig. 1A). False-positive rates due to sequencing errors (Fig. 1B) were higher for LoF variants than for missense and synonymous variants in the CHB+JPT and YRI populations

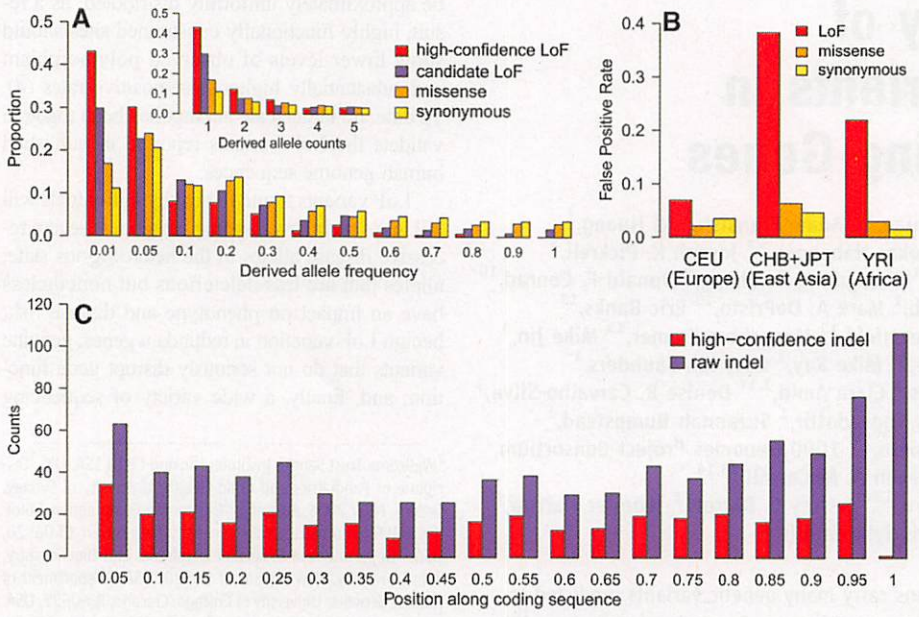

Fig. 1. (**A**) Derived allele frequency distribution in the CEU population for raw and high-confidence LoF variants, compared to missense and synonymous coding variants. (Inset) Distribution of the proportion of SNVs in each class at low allele counts (1 to 5). (**B**) False-positive rates (based on independent array genotyping) for LoF variants filtered for annotation artifacts and frequency-matched missense and synonymous SNVs. (**C**) Distribution of frameshift indels along the coding region of affected genes, before and after filtering.

Table 1. Numbers of LoF variants before and after filtering. Total numbers of candidate LoF variants and average number of LoF sites per individual (homozygous sites in parentheses) are shown for each LoF class. For large deletions, numbers represent total number of genes predicted to be inactivated.

Variant type	Before filtering					After filtering				
	Total	1000G low-coverage average per individual			NA12878	Total	1000G low-coverage average per individual			NA12878
		CEU	CHB+JPT	YRI			CEU	CHB+JPT	YRI	
Stop	1111	85.7 (21.8)	113.4 (26.7)	109.1 (23.7)	115 (25)	565	26.2 (5.2)	27.4 (6.9)	37.2 (6.3)	23 (2)
Splice	658	80.5 (29.5)	98.1 (35.6)	89.0 (30.4)	95 (32)	267	11.2 (1.9)	13.2 (2.5)	13.7 (1.9)	12 (1)
Frameshift indel	1040	217.8 (112.1)	225.5 (121.7)	247.2 (118.7)	348 (159)	337	38.2 (9.2)	36.2 (9.0)	44.0 (8.0)	38 (11)
Large deletion	142	32.4 (12.2)	31.2 (11.8)	31.4 (9.7)	31 (5)	116	28.3 (6.2)	26.7 (5.9)	26.6 (5.5)	24 (4)
Total	2951	416.4 (175.6)	468.2 (195.8)	476.7 (316.0)	654 (286)	1285	103.9 (22.5)	103.5 (24.3)	121.5 (21.7)	97 (18)